ACS APPLIED NANO MATERIALS

Open Access

www.acsanm.org

Article

Theranostic Nanoscaffold for Targeted Delivery of Cisplatin

Norma Lucia Buriticá Zuluaga, Gustavo Penteado Battesini Carretero, Yuli Yohana Serna Torres, Sergio Hiroshi Toma, Flavia Carla Meotti, Beatriz dos Santos Cugnasca, Koiti Araki, Alcindo Aparecido dos Santos, Henning Ulrich, Hernan Chaimovich, and Iolanda Midea Cuccovia*

Cite This: *ACS Appl. Nano Mater.* 2026, 9, 2204−2217

Read Online

ACCESS | Metrics & More | Article Recommendations | Supporting Information

ABSTRACT: The development of multifunctional nanoscaffolds offers a promising approach for the simultaneous diagnosis and therapy of various diseases. In this study, we designed and evaluated a multifunctional theranostic nanoscaffold termed FLAB, which consists of four integrated components: nanoparticles of iron oxide (Fe_3O_4) functionalized with polyethylenimine (F), liposomes (L), a targeting aptamer (A), and the fluorescent dye [2-(4-(5,5-difluoro-5*H* 4λ^4,5λ^4-dipyrrolo[1,2-c:2′,1′-f]-[1,3,2]diazaborinin-10-yl)phenoxy)ethan-1-ol] (BODIPY, B). Upon encapsulation of the chemotherapeutic agent cisplatin (c), the nanoscaffold is referred to as FLABc. This nanomodular design enables both targeted drug delivery and imaging capabilities, making FLAB and FLABc promising candidates for theranostic applications. While cisplatin was selected as a model chemotherapeutic agent for lung cancer treatment, the nanoscaffold can be readily adapted to deliver alternative drugs for other pathological conditions. The targeting aptamer, which can be substituted to recognize different molecular biomarkers, enables disease-specific delivery and enhances therapeutic precision. Physicochemical characterization confirmed successful assembly and stability of the nanoscaffold. Cytotoxicity assays performed on MRC-5 (normal lung fibroblasts) and H1299 (nonsmall cell lung carcinoma) demonstrated that FLABc effectively reduced cancer cell viability while minimizing the cytotoxicity typically associated with free cisplatin. Flow cytometry revealed high apoptosis induction in H1299 lung cancer cells, and fluorescence microscopy confirmed efficient cellular uptake and localization. BODIPY-labeled FLAB nanoscaffolds are partially internalized in vesicles of H1299 cells, indicating trafficking to late endosomes/lysosomes. This distribution may facilitate intracellular cisplatin release and enhance therapeutic activity. These findings support the potential of FLAB as a flexible and targeted theranostic tool, capable of integrating drug delivery and diagnostic capabilities in a single nanosystem for cancer and beyond.

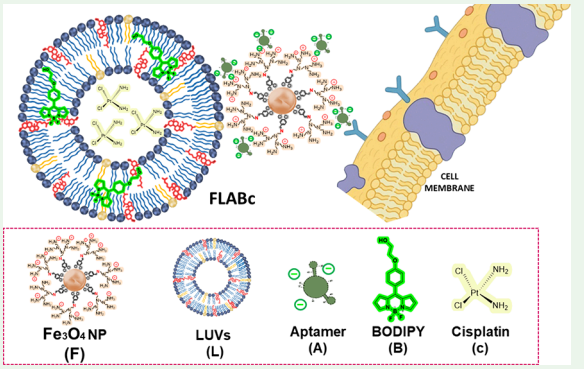

KEYWORDS: *theranostic, nanoscaffold, cisplatin, BODIPY, targeted drug delivery*

1. HIGHLIGHTS

- FLABc nanoscaffold boosts cisplatin efficacy by ∼100-fold in lung cancer cells.
- Enables lower cisplatin doses, reducing systemic toxicity significantly.
- Aptamer functionalization ensures selective targeting of tumor cells.
- Theranostic features allow simultaneous drug delivery and imaging.
- FLAB nanoscaffolds are partially internalized in vesicles of H1299 cells.

2. INTRODUCTION

Cancer is a group of diseases characterized by uncontrolled cell growth, invasion into surrounding tissues, and the potential to metastasize to distant organs. It remains one of the leading causes of morbidity and mortality worldwide, accounting for nearly 20 million new cases of cancer in 2022. Projections based on demographic trends estimate that cancer will affect up to 35 million new individuals annually by the year 2050.[1]

Among the various types of cancer, lung cancer is the most commonly diagnosed and the leading cause of cancer-related deaths globally. It is broadly categorized into nonsmall cell lung cancer (NSCLC), which constitutes about 85% of cases, and small cell lung cancer (SCLC).[2] Major risk factors include tobacco smoking, exposure to environmental pollutants, and genetic predisposition.

Treatment strategies for lung cancer depend on the cancer subtype, stage, and patient condition and often involve a

Received: October 7, 2025
Revised: January 13, 2026
Accepted: January 16, 2026
Published: January 28, 2026

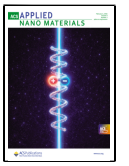

combination of surgery, radiotherapy, chemotherapy, targeted therapy, and, more recently, immunotherapy.[3] Chemotherapeutic agents like cisplatin, a platinum-based compound, are considered cornerstone treatments for many solid tumors, including NSCLC and SCLC. Cisplatin acts primarily by forming DNA adducts, which interfere with DNA replication and transcription, ultimately triggering apoptosis.[4]

Despite its effectiveness, the clinical use of cisplatin is severely limited by its dose-dependent toxicities, including nephrotoxicity, neurotoxicity, ototoxicity, and myelosuppression.[5] Moreover, the development of resistance mechanisms within tumor cells, such as increased DNA repair, drug efflux, and detoxification, reduces the therapeutic efficacy of the treatment.

To overcome these limitations, nanotechnology-based delivery systems, such as liposomes, polymeric nanoparticles, and micelles, have been developed to encapsulate cisplatin.[6−8] These systems aim to enhance drug solubility, improve pharmacokinetics, promote tumor-specific accumulation through enhanced permeability and retention (EPR) effects, and reduce systemic toxicity.[9] Encapsulated cisplatin formulations have demonstrated promising preclinical and clinical results, offering enhanced antitumor efficacy with a more favorable safety profile compared to free cisplatin.[10]

Liposome-based formulations, such as Lipoplatin, have reached the clinical trial stage, showed lower nephrotoxicity and improved tolerability while maintaining their anticancer efficacy.[11] These advances suggest that cisplatin, despite its limitations, remains key in cancer therapy, and nanotechnology offers new tools to unleash its full therapeutic potential, especially in complex malignancies such as lung cancer.

The search for more effective and less toxic cancer treatments has driven the development of innovative nanostructured platforms, which combine therapy and diagnostics in a single entity, and the development of multifunctional nanocarriers that address the main limitations of conventional chemotherapeutics, such as low solubility, rapid systemic clearance, lack of tumor selectivity, and severe nonspecific toxicity. Among the various materials investigated, iron oxide (Fe_3O_4) magnetic nanoparticles have attracted considerable attention due to their intrinsic superparamagnetic properties, biocompatibility, and facile surface functionalization. These features make them suitable for a broad spectrum of biomedical applications, such as targeted drug delivery, magnetic resonance imaging (MRI), and magnetic hyperthermia.[12] Despite their potential, uncoated Fe_3O_4 nanoparticles can induce cytotoxic effects in human cells due to their high surface reactivity and propensity to generate reactive oxygen species (ROS), which can compromise cell membranes and organelle integrity.[13] To mitigate these effects and improve biocompatibility, Fe_3O_4 nanoparticles can be integrated into liposomal structures. Liposomes, composed of biocompatible phospholipid bilayers, not only protect Fe3O4 from direct biological contact but also act as effective drug carriers capable of encapsulating both hydrophilic and hydrophobic agents.[14]

Liposomes can be functionalized with molecular recognition elements to enable active targeting. Among the recognition molecules, aptamers (synthetic single-stranded oligonucleotides) offer advantages over traditional antibodies, such as lower immunogenicity, ease of modification, and high target specificity.[15,16] When conjugated to liposomes, aptamers enable selective binding to specific tumor biomarkers, improving the accumulation of therapeutic cargo at the tumor site and reducing systemic toxicity.[17]

To further enhance the imaging capabilities of liposomal-magnetic nanoscaffolds, boron-dipyrromethene (BODIPY) fluorophores can be integrated into the lipid bilayer. BODIPY dyes are recognized for their photostability, high quantum yield, and tunable fluorescence, making them ideal for monitoring nanocarrier biodistribution and cellular uptake both in vitro and in vivo.[18,19] Combining BODIPY with aptamer-functionalized, magnetically responsive liposomes, a versatile theranostic platform emerges, capable of diagnosing and treating malignancies with high specificity.

We describe here a multifunctional hybrid nanoscaffold, named FLAB, comprising four synergistic components: Fe_3O_4 nanoparticles for magnetic responsiveness, liposomes as biocompatible drug carriers, BODIPY dye for fluorescence imaging, and an aptamer for cancer specific targeting ligand for selective binding to lung cancer cells. FLAB was loaded with cisplatin (FLABc) to enable targeted death of lung cancer cells in vitro. The Fe_3O_4 cores were functionalized with aldehyde groups and coated with polyethylenimine (PEI), which confers a positive surface charge for electrostatic assembly with negatively charged liposomes. These liposomes encapsulate cisplatin for its chemotherapeutic action. This integrated design seeks to enhance cellular uptake through receptor mediated endocytosis, prolong systemic circulation, and minimize unwanted effects. As a proof of concept, we demonstrated that FLABc was cytotoxic for cancer derived H1299 cells and did not affect the normal control i.e. MRC5 cell lines.

3. MATERIALS AND METHODS

3.1. Synthesis of Fe_3O_4 Nanoparticles (NPs)

Fe_3O_4 nanoparticles (NPs) were synthesized according to a previously described method.[20−22] The NPs surface was then functionalized with 3,4-dihydroxybenzaldehyde (CAS 139−85−5, Sigma-Aldrich) to introduce aldehyde groups (NPs-APC), a process adapted from Ferreira et al.[23] Subsequently, the aldehyde-functionalized nanoparticles were conjugated with polyethylenimine (PEI) (branched, Mw ∼ 25,000, CAS 9002−98−6). This coupling reaction occurred between the aldehyde groups on the NP surface and the amine groups of the PEI, forming imine (Schiff base) bonds (-C = N-) to covalently link the two components.[24]

3.2. Fluorescent BODIPY probe

The BODIPY derivative used in this study, (2-(4-(5,5-difluoro-5H-4λ^4,5 λ^4-dipyrrol[1,2-c:2′,1′-f][1,2,3]diazaborinin-10-yl)phenoxy)-ethan-1-ol, was synthesized following the procedure described in our previous work[25−27] (Supporting Information 1, Figure S1).

The BODIPY derivative exhibits an amphiphilic structure, consisting of an apolar fluorophore and a polar hydroxyl terminus. Due to its predominantly apolar character, it displays a strong affinity for hydrophobic compartments within the liposomal bilayer.

3.3. Aptamer, A254_10

The FAM-labeled aptamer **A254_10** (5′-FAM-**CCCTCATGTGTTGTTTTCGTATTTAAATATTATA**) was used in this study. This aptamer was originally selected for its high affinity toward A549 lung cancer cells, as described by Vidic et al.[28] The aptamer was synthesized with a 5′-FAM modification for fluorescence-based detection.

3.4. Aptamer Binding Assay by Flow Cytometry

To evaluate the binding capacity of the selected FAM-labeled aptamer to H1299 lung cancer cells, flow cytometry analysis was performed. For the binding assay, H1299 cells (with fewer than 10 passages) were cultured under standard conditions and harvested at approximately 80% confluence. A total of 2×10^5 cells were incubated with 500 nM of the FAM-labeled aptamer in 500 μL of binding buffer in 1.5 mL microcentrifuge tubes.

https://doi.org/10.1021/acsanm.5c04519
ACS Appl. Nano Mater. 2026, 9, 2204−2217

The cell-aptamer suspensions were incubated at room temperature for 45 min on a HulaMixer (Life Technologies) set to rotate at 90° to maintain gentle agitation and ensure uniform exposure. Following incubation, the cells were washed twice by centrifugation at 1200 rpm (118x g) for 5 min to remove unbound aptamer. After each centrifugation step, the supernatant was discarded, and the cell pellet was resuspended in a binding buffer. Untreated cells (no aptamer or fluorophore) served as the negative control, while cells stained with the hydrophobic BODIPY probe were used as the positive control to establish gating for the FITC channel, which corresponds to the emission of the FAM-labeled aptamer. BODIPY accumulates in intracellular membranes, providing a consistent fluorescence signal. Fluorescence was detected in the FITC channel (excitation at 488 nm, emission at 530 nm), and data were analyzed to assess the relative binding efficiency of the aptamer to H1299 cells.

3.5. Preparation and Characterization of Liposomes

Stock solutions of 0.01 M 1-palmitoyl-2-oleoyl-*sn*-glycero-3-phosphocholine (POPC), 1-palmitoyl-2-oleoyl-*sn*-glycero-3-phosphoglycerol (POPG), and cholesterol (CHOL), were prepared in chloroform. Lipids (Figure S2) were from Avanti Polar Lipids (Alabaster, AL, USA). The concentrations of the POPC and POPG solutions were determined using the Rouser method,[29] adapted by Manzini et al.[30] for phosphate quantification, while the CHOL concentration was determined gravimetrically. To prepare lipid films, appropriate volumes of the stock solutions were mixed in a 70:10:20 molar ratio (POPC: POPG: CHOL) in round-bottom glass tubes. The solvent was then removed by evaporation under a gentle stream of argon gas to prevent lipid oxidation, forming a thin lipid film along the inner wall of the tube, followed by vacuum desiccation for a minimum of 2 h to ensure complete solvent removal. The film was stored at −4 °C until further use.

The dried films were then hydrated with a 10 mM Tris-HCl buffer (Aldrich, St Louis, Mo, USA) (pH 7.4), followed by vortexing to disperse the lipids into multilamellar vesicles (MLVs). Large unilamellar vesicles (LUVs) (∼100 nm) were prepared by extruding MLVs through polycarbonate membranes using a LiposoFast syringe-driven extruder. LUVs were maintained under refrigeration (7 °C) and usually used the same day.

3.6. Spectroscopy and Binding Assays

Fluorescence measurements were performed using a Hitachi F7000 spectrofluorometer (Hitachi, Tokyo, Japan) equipped with a 450 W xenon lamp. Quartz cuvettes with a 1 cm path length were used, with both excitation and emission slit widths set to 3 nm. The excitation wavelength was 445 nm, and emission spectra were recorded from 450 to 650 nm at a scanning speed of 240 nm/min.

3.6.1. Binding Affinity Assay (Titration of Lipid into Fixed BODIPY). To determine the binding affinity between BODIPY and lipid membranes, a fixed concentration of BODIPY (10 μM) was incubated with increasing concentrations of LUVs. After each addition, fluorescence emission spectra were collected and the intensity at 520 nm was recorded. Spectra of buffer and LUVs (without BODIPY) were acquired and subtracted from the experimental data to correct for background fluorescence and scattering. Corrections were also applied for dilution and potential inner filter effects. The fraction of BODIPY associated with the membrane at each lipid concentration was calculated using the following equation:

$$\text{Fraction Bound}_{[L]} = (I_{[L]} - I_0)/(I_{\text{Max}} - I_0)$$

where I_0 is the Emission intensity at 520 nm in absence of lipid, $I_{[L]}$ Emission intensity at a given lipid concentration and I_{Max} Emission intensity at the highest lipid concentration.

3.6.2. Partition Assay (Titration of BODIPY into Fixed Lipid Concentration). In a complementary experiment, the partitioning behavior of BODIPY into lipid membranes was assessed by maintaining LUVs at a constant concentration of 200 μM, while increasing BODIPY concentration from 0 to 20 μM in 0.1 μM increments. After each addition, the fluorescence emission at 515 nm was recorded. Control spectra of LUVs and buffer (without BODIPY) were subtracted to correct for background. The partition isotherm was constructed by calculating the molar ratio of BODIPY to lipid (r) and plotting it against the free BODIPY concentration ($[\text{BODIPY}]_{Free}$). The apparent partition constant (K_{Ap}) was estimated from the initial slope using the equation:

$$r = K_{Ap}x[\text{BODIPY}]_{\text{Free}}$$

3.6.3. BODIPY−LUV Interaction in the Presence of Nanoparticles. To evaluate the effect of nanoparticles on BODIPY−membrane interactions, the partition experiment was repeated in the presence of Fe_3O_4 nanoparticles (60 μg/mL), maintaining the same protocol and concentration ranges for both BODIPY and LUVs. All fluorescence intensities were corrected for background and normalized where appropriate. Data analysis, curve fitting (nonlinear and segmented linear), and plotting were performed using OriginPro 2022 (OriginLab Corp., Northampton, MA).

3.7. Transmission Electron Microscopy

For the transmission electron microscopy (TEM) analysis, POPC:-POPG:CHOL 70:10:20 and Fe_3O_4 NP 10 μg/mL in 10 mM Tris-HCl, pH 7.4. A 5 μL droplet was deposited on a 300 mesh lacey carbon-coated copper grid (TED Pella) using an easyGlow discharge system (Pelco) with 15 mA negative current for 10 s. Specimens were analyzed in low-dose condition, with a defocus range of − 2 μm to − 4 μm, using a Jeol JEM-2100 (Pleasanton, USA) microscope equipped with a GATAN Orius SC1000A CCD camera, which features a 4008 × 2672 pixel resolution and high sensitivity for low-dose imaging, allowing for detailed visualization of nanoparticle-liposome interactions.

3.8. Analysis of Particles by Dynamic Light Scattering (DLS) and Zeta Potential

Values of average hydrodynamic diameter in dilute dispersions and zeta potential were obtained by dynamic light scattering measurements using a Zetasizer Nano ZS (Malvern Instruments, UK). In both cases, a helium−neon laser operating at 632.8 nm wavelength and about 20 mW was used. The experiments were performed at 25 °C and a scattering angle of 90° (q = 0.018 nm^{-1}). All the samples were measured in triplicate at room temperature.

A 1 mL sample of large unilamellar vesicles (LUVs) composed of POPC:POPG:CHOL (70:10:20 mol %) at a total lipid concentration of 200 μM was transferred to a quartz cuvette with a 1 cm path length to establish the baseline measurement. An aqueous suspension of Fe_3O_4 nanoparticles (100 μg/mL) was then added incrementally until a final LUVs-to-nanoparticle mass ratio of 1:1 was reached. The data obtained from this titration were used to construct a binding curve, from which the saturation point of liposome−nanoparticle interaction was determined. The ratio corresponding to surface saturation was identified as 0.4 (LUVs/NPs, w/w). After this determination, new experiments were initiated to characterize the resulting nanoscaffold. At the fixed saturation ratio, sequential additions of aptamers (2 μM) and BODIPY (0.1 μM) were performed. After each addition, measurements of hydrodynamic diameter and zeta potential were conducted to monitor the structural and surface property changes of the final formulation. All measurements were performed in triplicate, and the resulting data were plotted using Origin 2022.

3.9. Preparation and Purification of Cisplatin-Loaded Liposomes

Lipid films were prepared by evaporating a chloroform solution containing the desired lipid composition under reduced pressure to form a thin, uniform film on the inner surface of a round-bottom flask. The lipid film was then hydrated with 1 mL of cisplatin solution (50 μM) prepared in 0.01 M Tris-HCl buffer (pH 7.4), which served both to hydrate the lipids and to provide a standard for total cisplatin content. The hydration was carried out under gentle agitation at room temperature for 20 min, promoting the formation of multilamellar vesicles (MLVs) encapsulating cisplatin. To achieve a uniform size distribution and reduce vesicle size, the liposomal suspension was extruded through a polycarbonate membrane with a pore size of 100 nm using a mini-extruder system (Avanti Polar Lipids). The suspension was passed through the membrane at least 11 times to ensure

https://doi.org/10.1021/acsanm.5c04519
ACS Appl. Nano Mater. 2026, 9, 2204−2217

reproducibility and consistency in vesicle size. Subsequently, following the methodology of Carvalho Júnior et al.[31] the liposomal formulation was purified by ultracentrifugation at 150,000 × g for 1 h at 10 °C using a Beckman Coulter Optima ultracentrifuge to separate the unencapsulated cisplatin. The supernatant (300 μL), containing unencapsulated cisplatin, was carefully collected and stored for quantification using a colorimetric assay, as described in Section 2.10.

3.10. Quantification of Free Cisplatin in the Supernatant

The concentration of unencapsulated cisplatin present in the liposomal supernatant was determined using a colorimetric assay adapted from the protocol described by Basotra et al.[32] with minor modifications. Briefly, 10, 50, or 100 μL aliquots of the supernatant were transferred to Pyrex tubes and mixed with 250 μL of o-phenylenediamine (OPDA) solution (1.4 mg/mL in distilled water) and 500 μL of phosphate-buffered saline (PBS, pH 6.8). The reaction mixtures were incubated in a dry heat block at 100 °C for 10 min to facilitate the formation of a colored OPDA−cisplatin complex. Following incubation, the samples were cooled to room temperature, and 1.75 mL of dimethylformamide (DMF) was added to each tube. The samples were then incubated for an additional 10 min at room temperature. The resulting blue-colored complex was quantified by measuring the absorbance at 706 nm using a UV−Visible spectrophotometer (Thermo Scientific Evolution 220). A calibration curve was established using a series of standard cisplatin solutions prepared in the same buffer system, enabling quantification within the assay's detection range and determination of encapsulation efficiency (Figure S3). The percentage of encapsulated cisplatin was calculated by comparing the absorbance of samples collected before liposome hydration (total cisplatin) with that of the supernatant after ultracentrifugation (unencapsulated cisplatin). All measurements were conducted in triplicate. Negative control reactions containing all reagents except cisplatin were included to determine baseline absorbance and confirm assay specificity.

3.11. Filtration-Based Separation of Fe_3O_4 Nanoparticles with and without Aptamer Binding

Filtration was performed using an MF-Millipore membrane filter with a pore size of 0.025 μm, placed in a stainless-steel micro syringe filter holder. Initially, 1 mL of a solution containing carboxyfluorescein-labeled aptamer at a concentration of 0.1 μM in 0.01 M Tris-HCl buffer (pH 7.4) was filtered to confirm that the membrane did not retain the aptamer. Subsequently, 1 mL of a sample containing Fe_3O_4 nanoparticles (20 μg/mL) mixed with 0.1 μM aptamer in the same buffer was passed through the filter. The fluorescence of the eluates was measured at 517 nm (emission) after excitation at 490 nm, using a Synergy HT plate reader (Bio-Tek, Winooski, VT, USA). Additionally, the fluorescence of the buffer (as a baseline) and the Fe_3O_4 nanoparticle solution before filtration was measured for reference.

3.12. MTT Assay for Evaluating Cell Viability in HL-60 Cells

HL-60 cells were cultured in RPMI-1640 medium supplemented with 10% fetal bovine serum (FBS) and 1% penicillin-streptomycin. Cells were maintained at 37 °C in a humidified atmosphere with 5% CO_2. For the MTT assay, HL-60 cells were seeded into 96-well plates at a density of 5×10^4 cells per well in 100 μL of complete medium. Cells were treated with varying concentrations of compounds (Liposome, Fe_3O_4NP, and Liposome-Fe_3O_4NP) and incubated for 24 and 48 h. The tests were conducted in triplicate for each concentration. Control wells received buffer as treatment. After the incubation period, 10 μL of MTT solution (5 mg/mL in PBS) was added to each well and incubated for 4 h at 37 °C. Following incubation, 100 μL of DMSO was added to dissolve the formazan crystals. The absorbance (*Abs*) was measured at 570 nm using a Synergy HT plate reader (Bio-Tek, Winooski, VT, USA). Cell viability was expressed as a percentage relative to the control group. The percentage of viable cells was calculated using the formula:

$$\text{cell viability (\%)} = \left(\frac{\text{Abs of treated cell}}{\text{Abs of control cell}}\right) \times 100$$

Statistical analysis was performed using one-way ANOVA followed by Tukey's post hoc test, with significance set at $p < 0.05$.

3.13. Fluorescence Imaging and Quantification of Cell Death

To assess cell death by fluorescence microscopy, an additional 96-well plate was prepared under the same conditions as the previous cytotoxicity experiment. After 48 h of incubation with treatments, DAPI was added to each well at a final concentration of 0.5 μg/mL and incubated for 15 min at room temperature in the dark. Following incubation, cells were imaged using a Floid Cell Imaging Station (Thermo Fisher Scientific). Fluorescence settings were adjusted to detect DAPI-stained nuclei (blue channel) and BODIPY fluorescence (green channel). Image analysis was performed using Fiji (ImageJ) software. A consistent threshold was applied to all images to identify DAPI-positive nuclei (indicative of dead cells). The "Analyze Particles" tool was used to count both DAPI-positive and total cell nuclei. The percentage of dead cells was calculated as the ratio of DAPI-positive nuclei to the total number of nuclei per image field.

3.14. Cytotoxicity Assays in H1299 and MRC5 Cell Lines

Prof. Dr. Henning Ulrich (University of São Paulo, Brazil) provided H1299 human lung cancer cells and MRC-5 normal lung cells. Lung cancer cell lines were grown adherently and maintained in RPMI 1640 medium (Gibco), containing 10% fetal bovine serum, 1% L-glutamine (Stem Cell Technologies, Vancouver, British Columbia, Canada), 100 μg/L of streptomycin, and 100 U/mL of penicillin (Stem Cell Technologies), at 37 °C in 5% CO_2. MRC-5 line cells were grown adherently and maintained in Eagle's minimal essential Medium containing 10% fetal bovine serum, and 1% penicillin solution at 37 °C in 5% CO_2. All experiments were performed in 96-well plates. Cells were seeded onto the plates at a density of 6×10^3 cells per well and incubated for 24 h before the experiments to allow adherence to the bottom of the well. Samples containing different concentrations of cisplatin (c), FLAB (Fe_3O_4−Liposome-Aptamer- BODIPY) and FLABc were added in a serial dilution mode, and each concentration was tested in triplicate. The treated cells were incubated for 24, 48, and 72 h and, subsequently, MTT (10 μL/well of Sigma) was added and incubated with the cells for an additional 4 h. Following incubation, to dissolve the formazan crystals, 100 μL of acidified isopropanol (0.04 N HCl in isopropanol) was added to each well and mixed thoroughly, as described by Mosmann[33] and recommended in the protocol provided with the MTT Cell Growth Assay Kit.[34] Within 1 h of adding the solubilization solution, the absorbance was measured using a microplate reader (Biotek Synergy H1 Hybrid Microplate Reader). The absorbance (*Abs*) was recorded at a test wavelength of 570 nm, with a reference wavelength of 630 nm to correct for background interference. Each experiment was repeated three times. The cell proliferation was calculated using the equation:

$$\text{Cell proliferation (\%)} = \left(\frac{\text{mean Abs of treated cell}}{\text{mean Abs of control cell}}\right) \times 100$$

3.15. Determination of Cell Death Mechanism by Flow Cytometry

To further investigate the mechanism of cell death, H1299 cells were analyzed by flow cytometry. Cells were incubated under the following conditions: untreated control, treatment with staurosporine (1 mM, apoptosis control), treatment with hydrogen peroxide (H_2O_2, 500 μM, necrosis control), and treatment with the FLABc nanoscaffold. After 24 h of incubation, cells were stained with Annexin V-FITC and propidium iodide, following the manufacturer's instructions to discriminate between apoptotic and necrotic cells. Samples were analyzed using a CytoFLEX LX Analyzer flow cytometer. Data were processed using FlowJo software, and the percentage of viable, apoptotic, and necrotic cells was quantified.

3.16. Hemolytic Activity of FLAB, Cisplatin, and Their Combination

The hemolytic activity of compounds was assessed following the method described by Mojsoska et al.[35] Briefly, 5 mL of blood from healthy volunteers was diluted in 40 mL of sterile phosphate-buffered saline (PBS, 140 mM NaCl, 10 mM phosphate, pH 7.4) and centrifuged

https://doi.org/10.1021/acsanm.5c04519
ACS Appl. Nano Mater. 2026, 9, 2204−2217

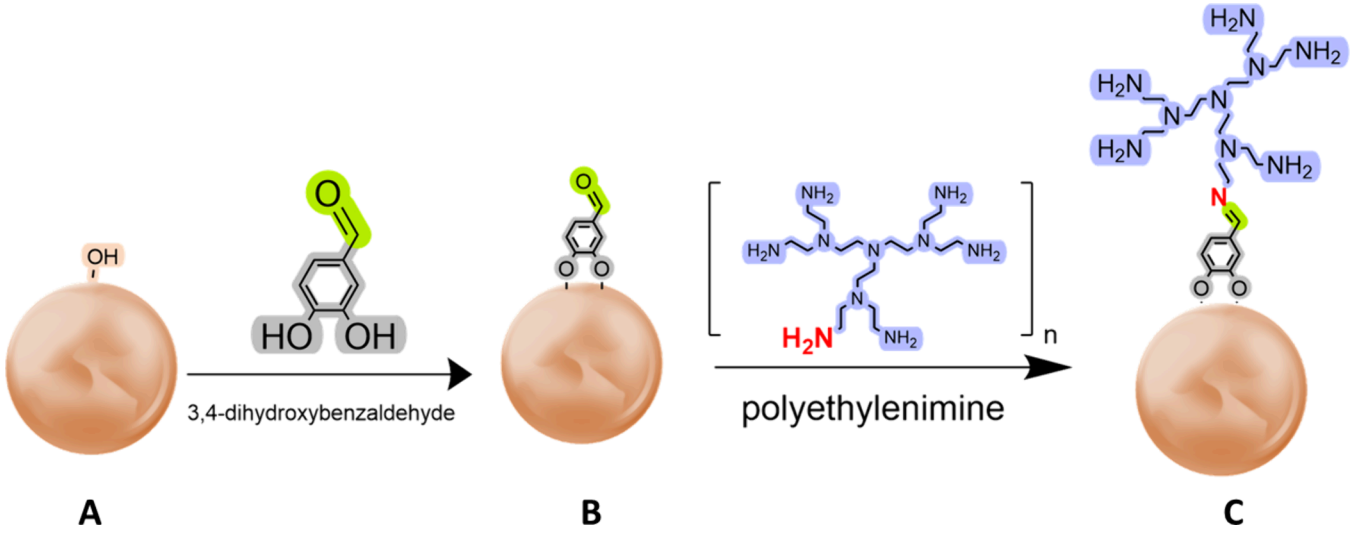

Figure 1. Schematic representation of Fe_3O_4 nanoparticles: (a) Fe_3O_4 core, (b) functionalization with aldehyde groups, and (c) final modification with polyethylenimine (PEI).

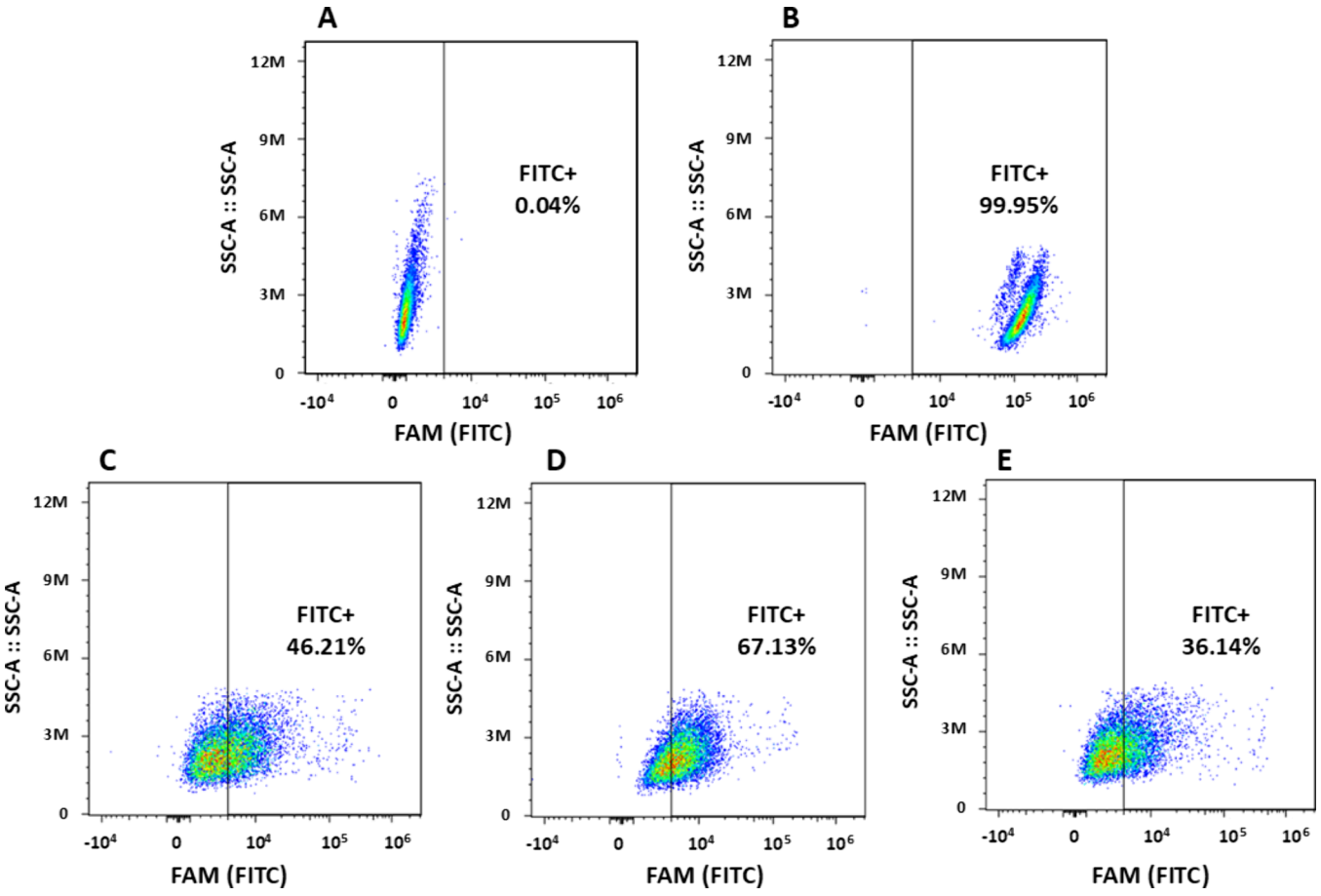

Figure 2. Dot plots show side scatter area (SSC-A) versus green fluorescence intensity (FAM fluorescence, FITC channel). A total of 10,000 events were recorded for each condition. (A) Negative control: untreated H1299 cells, used to determine background autofluorescence. (B) Positive control: H1299 cells incubated with BODIPY, a green fluorescent dye emitting in the FITC channel, used to define the R2 gate for FITC-positive cells. (C–E) Triplicates of H1299 cells incubated with the FAM-labeled aptamer A254_10.

at 1500 rpm (500x g) for 10 min. The supernatant was discarded, and the erythrocytes were washed three times with PBS. A 3% red blood cell (RBC) suspension was prepared by resuspending the cells in 9.7 mL of PBS. FLAB solutions (0.01–5 mM), cisplatin (0.07–80 μM) and FLAB+cisplatin (0.01–5 mM + 0.01–5 μM respectively) were prepared in a U-bottom 96-well polypropylene plate (Corning, NY, USA) with a final volume of 50 μL per well. Then, 50 μL of the RBC suspension was added to each well, yielding a final RBC concentration of 1.5%. PBS served as a negative control, while 0.1% (v/v) Triton X-100 (Sigma-Aldrich, MO, USA) was used as a positive control for complete hemolysis.

https://doi.org/10.1021/acsanm.5c04519
ACS Appl. Nano Mater. 2026, 9, 2204–2217

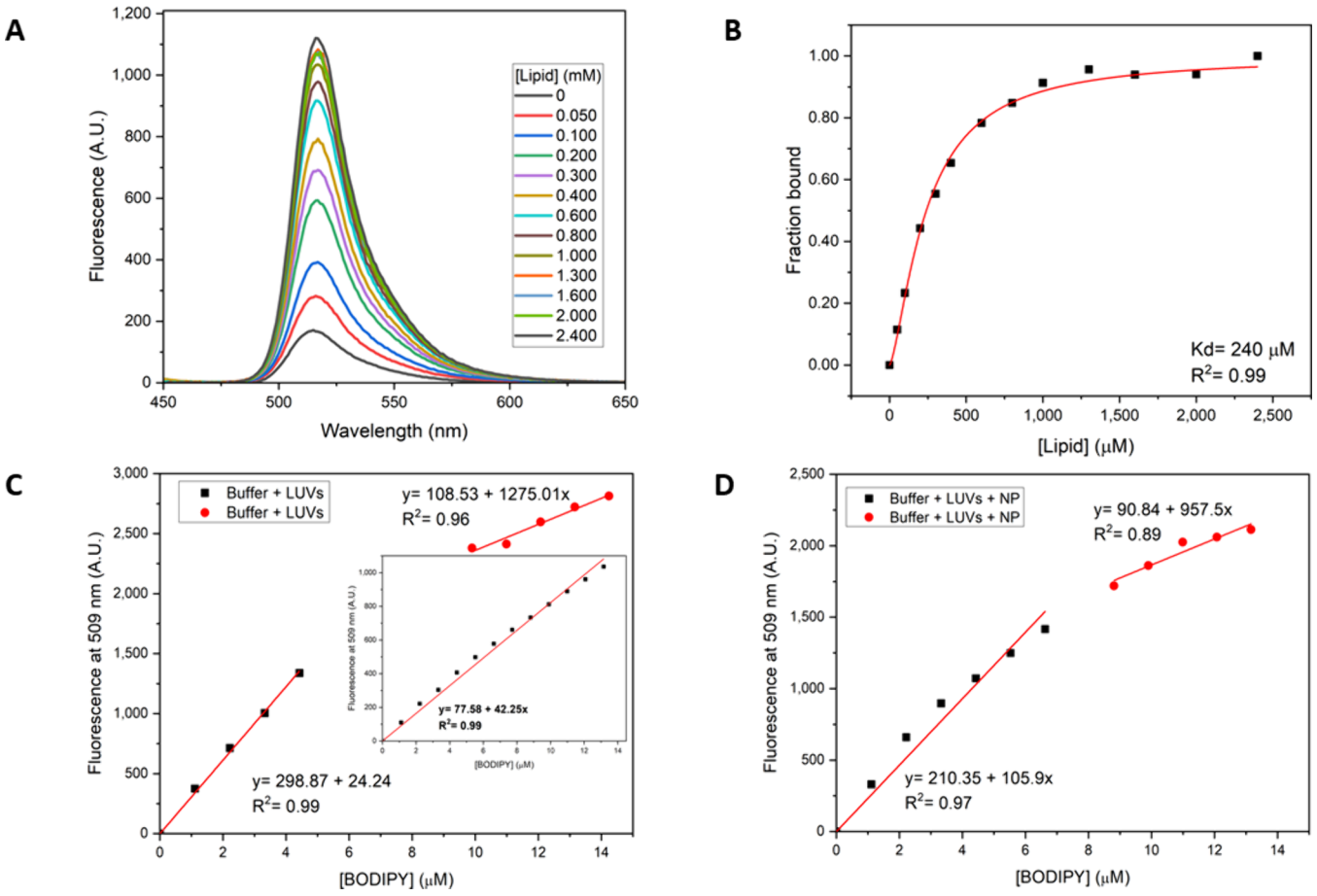

Figure 3. BODIPY internalization and binding to liposomes under different conditions (excitation at 445 nm). (A) Emission spectra of BODIPY in the presence of increasing concentrations of liposomes (0−2.4 mM). (B) Binding curve of BODIPY to liposomes, fitted using the Hill equation. The apparent dissociation constant (K_d) is 240 μM. (C) Linear relationship between BODIPY concentration and fluorescence intensity at 509 nm in buffer containing liposomes (200 μM). The inset shows the calibration curve of BODIPY in buffer alone (control). (D) Linear fluorescence response of BODIPY in the presence of liposomes (200 μM) and Fe_3O_4 nanoparticles (60 μg/mL).

The plate was incubated at 37 °C under shaking for 3 h, followed by centrifugation at 1200 rpm (400× g) for 10 min. The supernatant was transferred to a flat-bottom 96-well polystyrene plate (Greiner Bio-One, Kremsmünster, Austria), and absorbance at 540 nm was measured using a Synergy HT plate reader (Bio-Tek, Winooski, VT, USA). Hemolysis percentage (Hemolysis %) was calculated as

$$\text{Hemolysis (\%)} = 100 \times \left(\frac{\text{Abs}_{\text{SAMPLE}} - \text{Abs}_{\text{PBS}}}{\text{Abs}_{\text{TRITON}} - \text{Abs}_{\text{PBS}}}\right)$$

where Abs_{SAMPLE} is the absorbance of the treated sample, Abs_{PBS} is the absorbance of the negative control containing only PBS, and Abs_{TRITON} is the absorbance of the positive control (100% hemolysis).

3.17. Colocalization of FLAB Nanoscaffold with LysoTracker

To investigate whether the internalization of the FLAB nanoscaffold occurs via endocytosis and subsequent trafficking to acidic compartments, colocalization studies were performed using confocal fluorescence microscopy.

H1299 cells were seeded onto 8-well chamber slides (Thermo Fisher Scientific) at a density of 5.0×10^4 cells per well and allowed to adhere overnight under standard cell culture conditions. On the following day, cells were incubated with the FLAB nanoscaffold at a final concentration of 5 μM for 1 h at 37 °C.

After FLAB incubation, cells were treated with LysoTracker (Thermo Fisher Scientific) at a final concentration of 50 nM for 30 min to label acidic vesicles, including late endosomes and lysosomes. Subsequently, cells were gently washed with phosphate-buffered saline (PBS) and mounted with a glass coverslip.

Fluorescence images were acquired using a confocal laser scanning microscope equipped with a 40× objective (TissueFAXS Plus confocal TissueGnostics GmbH, Wien, Austria). BODIPY-labeled FLAB fluorescence was detected in the green channel, while LysoTracker fluorescence was detected in the red channel. Image merging and colocalization analysis were performed using ImageJ software.

4. RESULTS

4.1. Synthesis of Fe_3O_4 Nanoparticles

The synthetic strategy for covalently binding hyperbranched PEI to Fe_3O_4 nanoparticles was adapted from the process described previously.[36] The goal was to simplify the steps and chemical reactions to ensure a higher yield, improved reproducibility, and greater robustness. For this reason, 3,4-dihydroxybenzaldehyde (APC) was chosen as the bridging ligand. This choice exploited both the affinity of its catechol group for anchoring to Fe_3O_4 surfaces and the ability of its aldehyde group to form Schiff bases with the amines. The pristine Fe_3O_4 nanoparticles showed an average diameter of 10.8 ± 3.6 nm (PdI, 0.15). Upon the addition of the APC ligand, the hydrodynamic size increased to 22.9 ± 8.3 nm (PdI, 0.11). Finally, functionalization with polyethylenimine (PEI) resulted in positively charged nanoparticles with an average hydrodynamic size of 50.2 ± 15.5 nm (PdI 0.14) and a surface charge

https://doi.org/10.1021/acsanm.5c04519
ACS Appl. Nano Mater. 2026, 9, 2204−2217

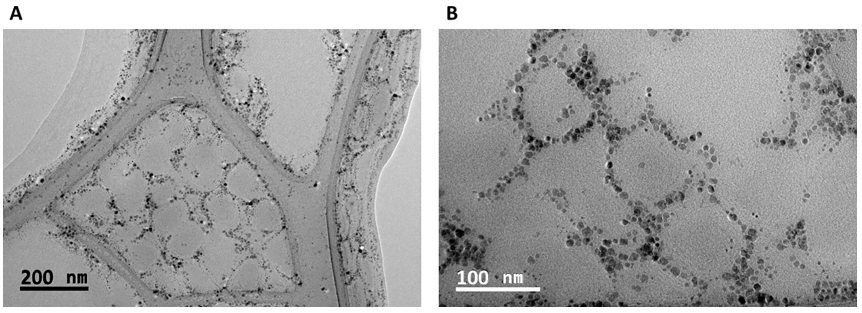

Figure 4. Positively charged nanoparticles binding to negatively charged liposomes. Transmission electron microscopy (TEM) images showing the interaction between cationic nanoparticles and anionic liposomes. (A) Nanoparticles densely bound to the surface of large unilamellar liposomes. (B) Higher magnification revealing nanoparticle clustering along liposome membranes. Scale bars: 200 (A) and 100 nm (B).

of +42 mV at pH 7.4. Figure 1 shows a schematic representation of the Fe_3O_4−NPs functionalization.

4.2. Aptamer Binding to H1299 Cells

Flow cytometry analysis was conducted to assess the binding efficiency of the FAM-labeled aptamer to H1299 lung cancer cells. Across three independent experiments, an average of 49.83% ± 12.92% of the 10,000 recorded events per assay exhibited fluorescence in the FITC channel, indicating successful aptamer binding (a typical result is shown in Figure 2). These findings suggest that the aptamer, initially selected against A549 cells, also demonstrates substantial affinity for H1299 cells.

Fluorescence intensities within the FITC+ gate (Figure 2) were 46.21%, 67.13%, and 36.14% across three independent experiments. The average percentage of FITC+ cells was 49.83% ± 12.92%. The R2 region (FITC+) was defined based on fluorescence thresholds established using negative (untreated cells) and positive (BODIPY-treated cells) controls.

4.3. Preparation and Characterization of Liposomes

Large Unilamellar Vesicles (LUVs) were prepared using POPC, POPG, and cholesterol in a 70:10:20 molar ratio. The average diameter was 98.3 ± 6 nm, polydispersity, PdI, 0.061 and the Zeta Potential was −32 ± 4 nm (Table S1). The stability of LUVs maintained under refrigeration (ca. 7 °C) was monitored for 39 days, measuring size and polydispersity (Table S1). No significant differences were observed in these parameters throughout the monitoring period, indicating that the vesicles remained stable under the experimental conditions (Table S1).

4.4. Fluorescence Based Analysis of BODIPY−Liposome Interaction

The interaction between BODIPY and lipid membranes was first evaluated by titrating increasing concentrations of liposomes into a fixed concentration of BODIPY (10 μM). As shown in Figure 3A (top left), the fluorescence emission of BODIPY increased progressively with lipid concentration, reaching a plateau at higher lipid levels. This increase in fluorescence intensity is consistent with the transition of BODIPY from an aqueous environment to a more hydrophobic lipid bilayer, which enhances its quantum yield. To quantify this interaction, the fluorescence intensity at 520 nm was used to calculate the fraction of BODIPY bound at each lipid concentration. The resulting binding isotherm (Figure 3B, top right) was fitted using a Hill equation, yielding an apparent dissociation constant (K_d) of approximately 243 μM, with a Hill coefficient of ∼ 1.44, suggesting a moderately cooperative binding process. These results indicate that BODIPY displays a specific and concentration-dependent association with the liposomal bilayer.

4.4.1. Determination of Liposome Saturation and Partition Behavior. To further characterize the membrane partitioning behavior, a complementary experiment was conducted in which BODIPY concentration was increased (0−20 μM) at a fixed lipid concentration (200 μM LUVs). The resulting fluorescence intensity at 515 nm displayed a biphasic profile (Figure 3C, bottom left). An initial linear increase in fluorescence was observed at low BODIPY concentrations, corresponding to efficient internalization of the dye into the liposome bilayer. A second, less steep linear segment emerged at higher BODIPY concentrations, indicating saturation of the liposomal membrane and accumulation of excess BODIPY in the aqueous phase. From this analysis, the saturation point of liposomes with BODIPY could be identified, and the slope of the first segment was used to estimate the apparent partition constant (K_{app}), reflecting the compound's preferential localization in the membrane phase relative to the buffer.

4.4.2. Effect of Fe_3O_4 Nanoparticles on BODIPY−LUV Interaction. To evaluate whether surface interactions with nanoparticles affect BODIPY−membrane partitioning, the same partition assay was repeated in the presence of Fe_3O_4 nanoparticles (60 μg/mL). As shown in Figure 3D (bottom right), the presence of nanoparticles did not significantly alter the biphasic behavior of the BODIPY−LUV system. Both the slopes and transition point between internalization and saturation phases remained comparable to the control (without nanoparticles), suggesting that Fe_3O_4 nanoparticles, likely bound to the liposomal surface via electrostatic interactions, do not interfere with the internalization or binding affinity of BODIPY.

4.5. Transmission Electron Microscopy

The interaction between Fe_3O_4 nanoparticles and liposomes was confirmed through transmission electron microscopy (TEM) imaging. Due to the high electron density of iron, Fe_3O_4 nanoparticles appear as small dark spots distributed along the surface of the liposomes (Figure 4). In contrast, the larger, clear vesicular structures correspond to LUVs, with an average diameter of approximately 100 nm. The observed small Fe_3O_4 nanoparticles distribution suggests electrostatic-driven association with the liposomal outer interface.

4.6. Analysis of Particles by Dynamic Light Scattering (DLS) and Zeta Potential

The interaction between negatively charged liposomes and Fe_3O_4 NPs was assessed using dynamic light scattering (DLS). Successive additions of Fe_3O_4 NPs led to progressive changes in both hydrodynamic diameter and zeta potential. A plateau in

https://doi.org/10.1021/acsanm.5c04519
ACS Appl. Nano Mater. 2026, 9, 2204−2217

zeta potential was observed at a liposome to nanoparticle (NPs/LUVs) mass ratio of 0.4, indicating saturation (Figure S4).

Similarly, the surface charge, initially negative, became positive due to the electrostatic interaction between the liposomes and Fe_3O_4 nanoparticles, as reflected in the zeta potential measurements (Table 1).

Table 1. Size, PDI, and Zeta Potential of Nanoparticles (The Concentrations of All NP Components Are in the Table Legend)[a]

composition of the nanoparticles (1)	size (nm)	PdI	zeta potential (mV)
LUVs	98 ± 2	0.06	−32 ± 3
LUVs + Fe_3O_4 NPs	160 ± 5	0.15	26 ± 6
LUVs + Fe_3O_4 NPs + aptamer	191 ± 12	0.24	22 ± 2
LUVs + Fe_3O_4NPs + aptamer + BODIPY	231 ± 10	0.23	22 ± 4

[a]LUVs = 200 μM; Fe_3O_4NPs = 6 μg/mL; Aptamer = 10 nM; BODIPY = 100 nM.

The size and surface charge of the LUVs were progressively altered following the sequential addition of Fe_3O_4 NPs, aptamers, and BODIPY.

The characterization of the liposomal formulation revealed large, well-defined unilamellar vesicles (LUVs) with a hydrodynamic diameter of ∼ 98 nm and low polydispersity (PdI < 0.1), which fits within the optimal size range for passive tumor targeting through the enhanced permeability and retention (EPR) effect. The addition of Fe_3O_4 NPs led to an increase in hydrodynamic diameter and a shift in zeta potential, consistent with electrostatic interactions and surface adsorption onto the vesicles. Such changes are characteristic of colloidal complex formation driven by electrostatic binding, as discussed by Honary and Zahir.[37] Saturation was reached at a defined LUV/NP ratio, consistent with complete coverage of the liposomal surface, as corroborated by transmission electron microscopy. The electron-dense Fe_3O_4 NPs remained associated with the liposomal membrane rather than being internalized, thus maintaining the compartmentalized architecture of the vesicles.

4.7. Encapsulation and Quantification of Cisplatin in Liposomes

Liposomes of POPC:POPG:CHOL (70:10:20) were prepared by hydrating a dried lipid film with a cisplatin solution (50 μM) in 0.01 M Tris-HCl buffer (pH 7.4), followed by extrusion through 100 nm polycarbonate membrane. The resulting liposomes exhibited an average hydrodynamic diameter of 98.2 ± 0.7 nm, as determined by dynamic light scattering (DLS), confirming the formation of a homogeneous population of large unilamellar vesicles (LUVs). To quantify the encapsulated cisplatin, the concentration of unencapsulated drug in the liposomal supernatant was determined using a colorimetric assay based on the reaction of cisplatin with o-phenylenediamine (OPDA) (see Materials and Methods). A calibration curve, constructed from serial dilutions of cisplatin standards (Figure S3), was used to determine the drug concentration in the supernatant and calculate the encapsulation efficiency. Absorbance readings for samples containing 10 μL of either the supernatant or cisplatin standard were below the assay's limit of detection and were therefore excluded from analysis. For larger volumes (50 and 100 μL), measurable absorbance signals were observed for both the cisplatin standard and the liposomal supernatant following ultracentrifugation. Comparison of absorbance values at 706 nm between the pre-encapsulation cisplatin solution and the postultracentrifugation supernatant revealed that approximately 81 ± 5% of the total cisplatin remained unencapsulated. This percentage corresponds to an encapsulation efficiency of 19 ± 5%. These findings indicate that under the current formulation and processing conditions, cisplatin is incorporated into the liposomal bilayers.

4.8. Filtration-Based Separation of Fe_3O_4 Nanoparticles with and without Aptamer Binding

The carboxyfluorescein-labeled aptamer (Aptamer-FAM) was used to monitor the interaction between the aptamer and Fe_3O_4 nanoparticles via a filtration-based retention assay (Figure S5). The absorbance of the Aptamer-FAM solution remained unchanged before and after filtration through an MF-Millipore membrane, indicating that the membrane did not retain the free aptamer. In contrast, when the aptamer was mixed with Fe_3O_4 nanoparticles prior to filtration, the absorbance of the eluate was comparable to that of the buffer (blank), suggesting that neither

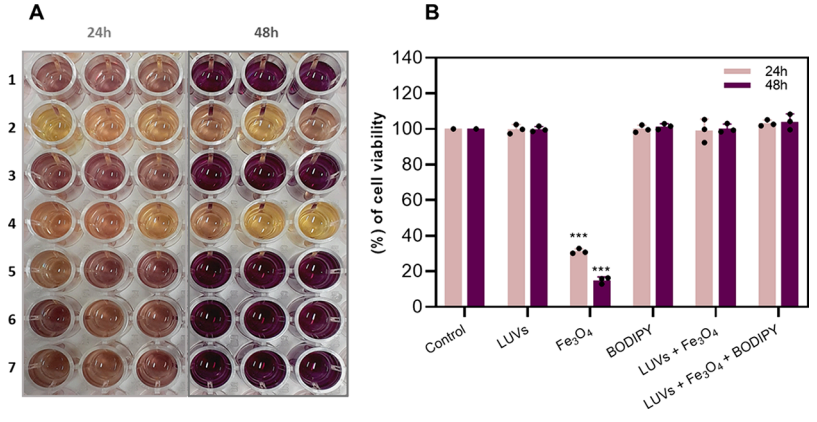

Figure 5. Relative fluorescence intensity of: (A) MTT colorimetric assay performed in triplicate to assess HL-60 cell viability after 24 and 48 h of treatment with the following formulations: (1) Negative control (RPMI-1640 medium), (2) positive control (Triton X-100), (3) LUVs (200 μM), (4) Fe_3O_4 NPs (6 μg/mL), (5) BODIPY (10 μM), (6) LUVs (200 μM) + Fe_3O_4 NPs (6 μg/mL), (7) LUVs (200 μM) + Fe_3O_4 NPs (6 μg/mL) + BODIPY (10 μM). (B) Quantitative analysis showing the percentage of viable HL-60 cells at 24 and 48 h for each condition. Data are presented as mean ± SD (n = 3). ***p < 0.001 vs all other treatment groups at the same time point (One-way ANOVA followed by Tukey's post hoc test).

https://doi.org/10.1021/acsanm.5c04519
ACS Appl. Nano Mater. 2026, 9, 2204−2217

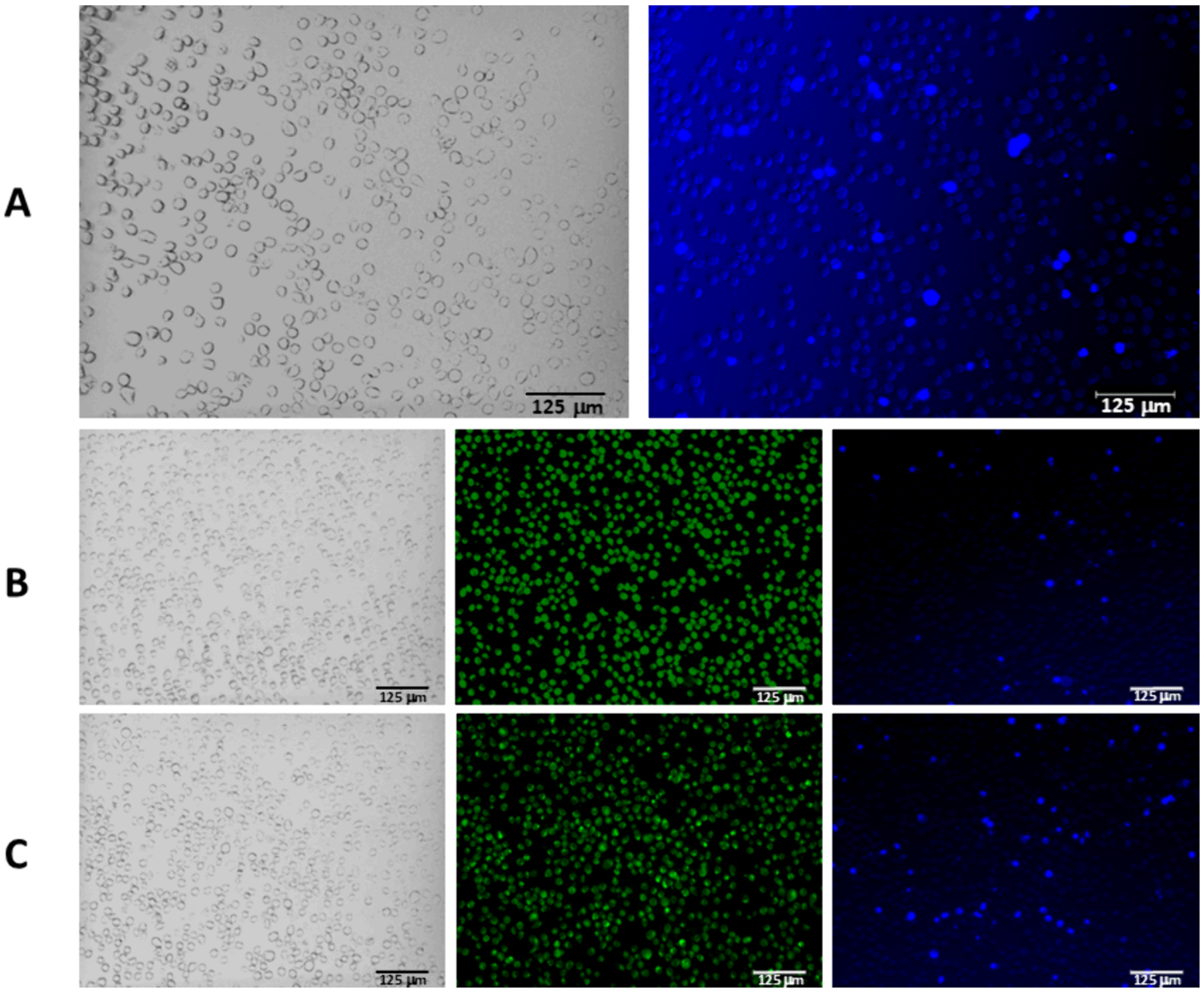

Figure 6. Cytotoxicity assessment of compounds in HL-60 cells. Representative micrographs of HL-60 cells under different treatment conditions, imaged using brightfield and fluorescence microscopy. (A) Negative control: cells stained only with DAPI (blue), which labels nuclei. (B) Cells treated with BODIPY-labeled compound and DAPI, showing clear BODIPY internalization (green fluorescence). (C) Cells treated with FLAB (nanoscaffold formulation) and DAPI, to evaluate the biocompatibility of the FLAB system. Each panel shows a brightfield image (left), BODIPY fluorescence (green, middle), and DAPI fluorescence (blue, right). Scale bars: 125 μm. Quantification of fluorescence intensity and cell counts was performed using ImageJ.

the nanoparticles nor the aptamer passed through the membrane. This result supports the interaction between the aptamer and the Fe_3O_4NPs, forming a stable complex that was retained by the membrane due to its pore size, preventing their passage (Figure S5).

The filtration experiment further demonstrated strong binding interactions between the aptamer and the Fe_3O_4NPs. The retention of both components by the membrane filter suggests stable complex formation, likely through electrostatic and hydrogen-bonding interactions between the amine-rich PEI-coated Fe_3O_4 and the phosphate backbone of the aptamer (S6).

4.9. MTT Assay for Evaluating Cell Viability in HL-60 Cells

To determine a nontoxic concentration range of the nanocarrier components prior to drug loading, undifferentiated HL-60 cells were employed as an initial screening model. These suspension cells are well established in cytotoxicity assays due to their rapid growth, ease of culture, and high sensitivity to chemical and nanomaterial-induced stress, providing reproducible data suitable for early stage toxicological evaluation.[38] This approach allowed us to define safe working concentrations for the lipid, BODIPY and iron oxide nanoparticle before application to adherent cancer cell lines. LUVs alone (200 μM) were not toxic to HL-60 cells, with cell viability remaining comparable to that of untreated controls. Treatment of HL-60 cells with 10 μg/mL Fe_3O_4 nanoparticles reduced cell viability to approximately 30%, indicating a significant toxic effect. However, when Fe_3O_4 nanoparticles were combined with LUVs or LUVs-BODIPY, cell viability increased markedly, reaching 98% relative to the untreated control group (Figure 5). These results suggest that the lipid vesicles effectively shield the cells from the cytotoxic effects of the iron oxide nanoparticles, demonstrating a protective role of the LUVs in HL-60 cells.

https://doi.org/10.1021/acsanm.5c04519
ACS Appl. Nano Mater. 2026, 9, 2204−2217

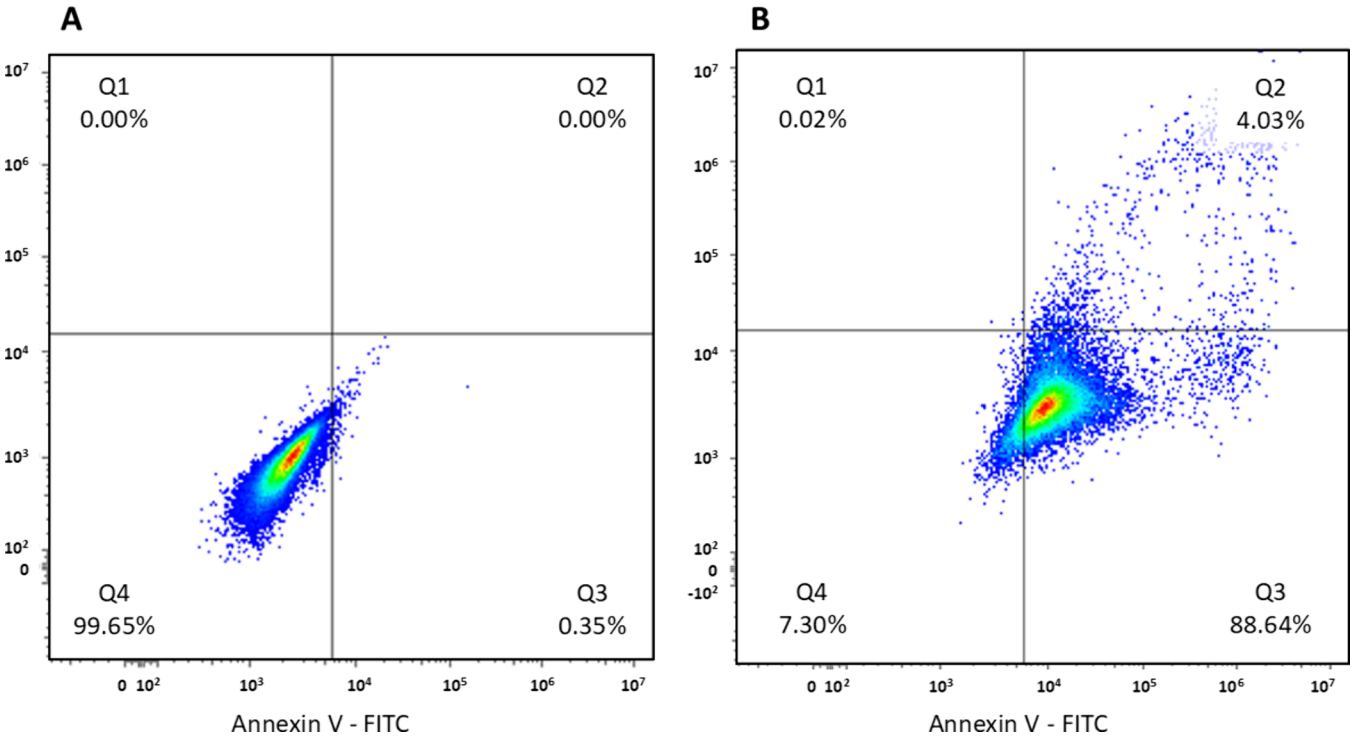

Figure 7. Flow cytometry analysis of H1299 cells using Annexin V and propidium iodide (PI) staining after treatment with FLABc (0.5 μM) for 48 h. (A) Untreated control cells. (B) Cells treated with FLAB/cisplatin.

4.10. Fluorescence Imaging and Quantification of Cell Death

To assess the cytotoxicity of the FLAB nanoscaffold in HL-60 cells, cells were incubated under three different conditions: untreated control, treatment with BODIPY alone, and treatment with FLAB. After 48 h of incubation, DAPI staining was used to identify nonviable (dead) cells. Fluorescence images were acquired using a Floid imaging system and analyzed with Fiji software, applying a consistent threshold to count total and DAPI positive nuclei.

Cell death was quantified by photomicrograph analysis (Figure 6), considering 5 random fields per well in 3 independent biological replicates, acquired with a 40x objective. The percentages of cell death were determined from the count of total cells (labeled with BODIPY) and dead cells (labeled with DAPI) in each field. For each biological replicate, the average of the five fields was calculated, and the averages of the replicates were used for statistical analyses. The results show that cell death was 7.71 ± 0.42% in the Control group, 6.10 ± 0.39% in the BODIPY-treated group, and 7.76 ± 0.39% in the Liposome-Fe3O4-BODIPY group. No statistically significant differences were observed between the groups (ANOVA, $p > 0.05$). These data indicate that both the free dye and the liposomal formulation containing iron oxide nanoparticles did not increase cell death compared to the control, suggesting good biocompatibility of the tested systems.

Functionally, the FLAB platform displayed excellent biocompatibility in HL-60 leukemia cells, showing no significant cytotoxicity from either the nanoscaffold or the fluorescent label alone. We confirmed this result by quantitative DAPI staining assays, which showed negligible differences in cell death compared to untreated controls.

4.11. Cytotoxicity of FLAB and FLABc in H1299 and MRC-5 Cells

To evaluate the cytotoxicity of the FLAB nanoscaffold and its capacity to potentiate cisplatin activity, MTT assays were conducted in human lung cancer cells (H1299) and normal lung fibroblasts (MRC-5). The empty FLAB scaffold exhibited minimal toxicity in both cell lines, with IC_{50} values of 480 ± 2.1 μM (H1299) and 500 ± 10 μM (MRC-5), confirming its biocompatibility and suitability as a drug carrier. Free cisplatin showed IC_{50} values of 10.5 ± 0.8 μM in H1299 and 20 ± 1.3 μM in MRC-5 cells, consistent with its known cytotoxic profile. Notably, encapsulation of cisplatin within FLAB (FLABc) markedly enhanced its potency in H1299 cells, lowering the IC_{50} to 0.1 ± 0.01 μM, representing an approximately 100-fold increase in efficacy compared to free cisplatin. In contrast, FLABc displayed an IC_{50} of 490 ± 13.4 μM in MRC-5 cells, comparable to the empty scaffold and substantially higher than that of free cisplatin, indicating pronounced selectivity toward cancer cells (Table S2).

4.12. Determination of Cell Death Mechanism by Flow Cytometry

Flow cytometry analysis using annexin V-FITC and PI staining demonstrated that treatment of H1299 cells with 0.5 M cisplatin-encapsulated FLABc for 48 h induced extensive apoptosis, Figure 7. The majority of cells (88.65%) were annexin V-positive/PI-negative (early apoptotic, Q3), while an additional 4.03% were annexin V-positive/PI-positive (late apoptotic, Q2). Only 7.30% of the cells remained viable (no staining, Q4) and 0.016% had necrosis (Q1). These findings confirm a strong pro-apoptotic effect of the FLABc nanocomposite, with minimal necrosis.

https://doi.org/10.1021/acsanm.5c04519
ACS Appl. Nano Mater. 2026, 9, 2204−2217

4.13. Hemolytic Activity of FLAB, Cisplatin, and Their Combination

The hemolytic potential of FLAB, cisplatin, and their combination was assessed using a red blood cell (RBC) assay (Figure S6). The tested concentrations included up to 80 μM for cisplatin, 5 mM for FLAB, and a 1:1 mixture of FLAB and cisplatin (FLABc, 5 mM/5 μM). Following incubation with RBCs, the release of hemoglobin into the supernatant (caused by cell lysis) was visually detected by the appearance of red coloration in the wells. Darker red shades indicate greater hemolysis. After incubation, the supernatants were transferred to a fresh 96-well plate, and free hemoglobin was quantified by measuring absorbance at 540 nm. The image shown is representative of three independent experiments with consistent results across replicates (Figure S6).

Cisplatin alone showed no hemolytic activity at any tested concentration. In contrast, FLAB alone induced concentration-dependent hemolysis, with 45% hemolysis observed at 2,500 μM, while no significant hemolysis was detected at 1,250 μM. The combination of FLAB and cisplatin also exhibited concentration-dependent hemolysis. At 1,250 μM FLAB/1.25 μM cisplatin, 12% hemolysis was observed, while no hemolysis occurred at 625 μM/0.625 μM (Figure S6). Importantly, at the concentration used in the cell-based experiments (100 μM FLAB/0.1 μM cisplatin, no hemolytic activity was detected. This suggests that the formulation is nonhemolytic and potentially safe for further biological applications.

4.14. Lysosomal Colocalization of FLAB Nanoscaffold

Confocal fluorescence microscopy was employed to investigate the intracellular trafficking and lysosomal localization of the FLAB nanoscaffold in H1299 cells. The BODIPY-labeled FLAB nanoscaffold exhibited a punctate green fluorescence pattern within the cytoplasm, consistent with vesicular internalization (Figure 8, FLAB). LysoTracker staining revealed discrete red fluorescent vesicles corresponding to acidic intracellular compartments, such as late endosomes and lysosomes (Figure 8, LysoTracker).

Merged images demonstrated partial overlap between the green FLAB signal and the red LysoTracker signal, resulting in yellow fluorescence in specific intracellular regions (Figure 8, merged). This colocalization pattern indicates that a fraction of the internalized FLAB nanoscaffold is trafficked to lysosomal compartments following cellular uptake.

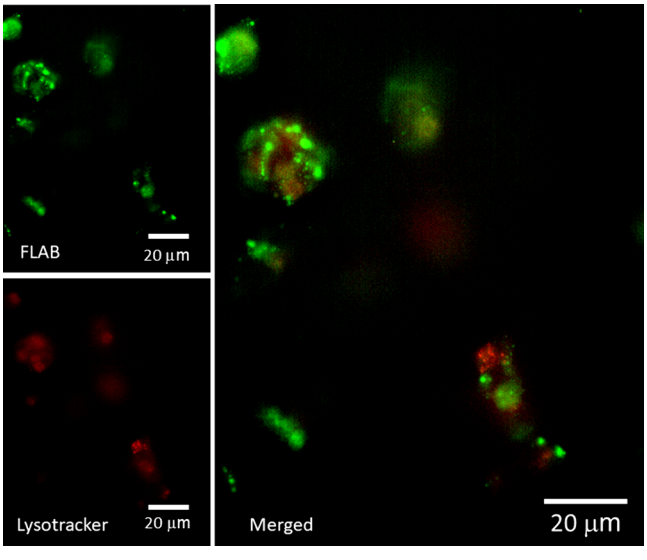

Figure 8. Colocalization of FLAB (Green), LysoTracker (Red), and merged images.

5. DISCUSSION

The design of multifunctional nanocarriers combining diagnostic and therapeutic modalities, commonly referred to as theranostic platforms, has emerged as a powerful approach to enhance the specificity and efficacy of anticancer treatments while minimizing systemic toxicity.[39,40] Our study introduces a multifunctional theranostic nanoscaffold (FLAB), designed to enhance cisplatin delivery to lung cancer cells. Notably, the colocalization of of FLAB (Green) and LysoTracker (Red) was not complete, as a significant portion of the FLAB signal remained spatially distinct from LysoTracker-positive vesicles. This observation suggests that, while FLAB is internalized predominantly via endocytic pathways, a subset of the nanoscaffold may reside in nonacidic compartments or undergo partial escape from the endolysosomal system. Such intracellular distribution may be relevant for the intracellular release of cisplatin by FLABc and its subsequent therapeutic activity.

The FLAB encapsulated cisplatin demonstrated a greater potency compared to free cisplatin in H1299 cells, implying a significant improvement in drug efficacy. Such enhanced effectiveness can be attributed to several synergistic mechanisms. Liposomes provide a biocompatible, protective bilayer vehicle that improves drug circulation time, reduces nonspecific distribution, and exploits the EPR effect for tumor accumulation.[41] The aptamer functionalization enables active targeting, promoting receptor-mediated uptake by tumor cells and minimizing off target delivery.[42] By combining these targeted liposomes with Fe_3O_4NPs, FLAB further enhances intracellular delivery through magnetic guidance and may generate reactive oxygen species (ROS) via iron-mediated Fenton reactions, which can amplify cytotoxicity selectively in the tumor microenvironment.[43] Importantly, the integration of these components enabled effective treatment of cancer cells at much lower cisplatin doses, thereby substantially reducing systemic exposure.

Given cisplatin effects are tempered by a well-documented and severe toxicity profile, making dose reduction essential for patient safety. According to Elmorsy et al.,[44] the drug is associated with dose-dependent and cumulative nephrotoxicity, leading to acute renal failure in a significant number of patients.[45] In addition to kidney damage, cisplatin frequently causes peripheral neuropathy, severe nausea and vomiting, and myelosuppression, which leads to potentially dangerous reductions in blood cell counts.[46] Given these serious side effects, reducing the effective dose of cisplatin is not just beneficial, it is clinically imperative.

Our data show that when cisplatin is encapsulated within the multifunctional FLAB nanoscaffold, (Liposomes, Fe_3O_4 nanoparticles, BODIPY fluorophores, and a specific tumor-targeting aptamer) its anticancer efficacy improves by approximately 100-fold compared to free cisplatin.[47] This enhancement allows for a dramatic reduction in required dosage, potentially lowering the risk of cumulative renal, auditory, neurological, and hematological toxicity. By delivering cisplatin more directly to tumor cells and minimizing off-target distribution, the FLAB platform could allow oncology practitioners to deliver effective therapy with significantly reduced systemic dose. This strategy aligns with established clinical goals: maintaining therapeutic benefit

https://doi.org/10.1021/acsanm.5c04519
ACS Appl. Nano Mater. 2026, 9, 2204−2217

while reducing the frequency and severity of adverse events, ultimately improving patient quality of life and outcomes

The selectivity of FLABc was further evidenced by its markedly lower cytotoxicity in MRC-5 normal lung fibroblasts, suggesting that the aptamer component effectively discriminates between malignant and nonmalignant cells. This finding aligns with previous studies reporting that aptamer-functionalized nanocarriers reduce off-target toxicity by preferentially binding to overexpressed biomarkers on tumor cells.[48,49] Such selectivity is crucial for enhancing the therapeutic index of anticancer drugs and improving patient outcomes in clinical settings.

Moreover, the inclusion of BODIPY dyes and Fe_3O_4 nanoparticles endows the FLAB system with theranostic potential, enabling real-time tracking and imaging alongside therapeutic delivery. The amphiphilic nature of BODIPY (featuring an apolar fluorophore core and a polar hydroxyl terminus) facilitated its efficient incorporation into the liposomal bilayer, as confirmed by fluorescence spectroscopy. The observed changes in fluorescence behavior upon incorporation indicate a shift in the microenvironment polarity, a hallmark of successful membrane integration of BODIPY dyes. Importantly, the attachment of Fe_3O_4 nanoparticles to the liposome surface did not interfere with BODIPY internalization, supporting the structural integrity and compartmentalization of the liposomal scaffold. This multifunctional design aligns with contemporary approaches in precision medicine, where therapeutic strategies are tailored to tumor-specific characteristics while incorporating diagnostic capabilities to monitor treatment efficacy in real time.[50,51]

6. CONCLUSIONS

The FLAB nanoscaffold represents a potential and significant advancement in cisplatin delivery for lung cancer treatment, combining enhanced efficacy, reduced systemic toxicity, and imaging capability. Confocal imaging in H1299 cells shows BODIPY-labeled FLAB nanoscaffolds are internalized in vesicles and partially colocalize with LysoTracker-labeled acidic compartments, indicating trafficking to late endosomes/lysosomes. The colocalization is incomplete, suggesting a substantial fraction resides in nonacidic compartments or escapes the endolysosomal pathway. This distribution may facilitate intracellular cisplatin release and enhance therapeutic activity. Future *in vivo* studies will be essential to validate these findings and assess the pharmacokinetics, biodistribution, and safety profile of this novel theranostic agent.

■ ASSOCIATED CONTENT

Supporting Information

The Supporting Information is available free of charge at https://pubs.acs.org/doi/10.1021/acsanm.5c04519.

Additional information on lipid and fluorescent probe structures; standard curve for cisplatin determination; stability, size, and zeta potential of the liposomes; filtration experiments determining aptamer/nanoparticle binding; IC_{50} values for H1299 and MRC5 cells treated with nanoscaffolds and cisplatin formulations; effect of the nanoparticles on red blood cell stability (PDF)

■ AUTHOR INFORMATION

Corresponding Author

Iolanda Midea Cuccovia − *Departamento de Bioquímica, Instituto de Química, Universidade de São Paulo, São Paulo 05508-900, Brazil;* orcid.org/0000-0001-8285-7419; Email: imcuccov@iq.usp.br

Authors

Norma Lucia Buriticá Zuluaga − *Departamento de Bioquímica, Instituto de Química, Universidade de São Paulo, São Paulo 05508-900, Brazil;* orcid.org/0000-0002-2912-2736

Gustavo Penteado Battesini Carretero − *Departamento de Química Fundamental, Instituto de Química, Universidade de São Paulo, São Paulo 05513-970, Brazil;* Present Address: Department of Science and Environment, Roskilde University, 4000 Roskilde, Denmark (G.P.B.C.); orcid.org/0000-0001-7776-6256

Yuli Yohana Serna Torres − *Departamento de Bioquímica, Instituto de Química, Universidade de São Paulo, São Paulo 05508-900, Brazil;* orcid.org/0009-0007-2850-4904

Sergio Hiroshi Toma − *Departamento de Química Fundamental, Instituto de Química, Universidade de São Paulo, São Paulo 05513-970, Brazil;* orcid.org/0000-0002-3003-7889

Flavia Carla Meotti − *Departamento de Bioquímica, Instituto de Química, Universidade de São Paulo, São Paulo 05508-900, Brazil;* orcid.org/0000-0002-7217-3352

Beatriz dos Santos Cugnasca − *Departamento de Química Fundamental, Instituto de Química, Universidade de São Paulo, São Paulo 05513-970, Brazil;* orcid.org/0000-0001-9924-8214

Koiti Araki − *Departamento de Química Fundamental, Instituto de Química, Universidade de São Paulo, São Paulo 05513-970, Brazil;* orcid.org/0000-0003-3485-4592

Alcindo Aparecido dos Santos − *Departamento de Química Fundamental, Instituto de Química, Universidade de São Paulo, São Paulo 05513-970, Brazil;* orcid.org/0000-0003-0358-610X

Henning Ulrich − *Departamento de Bioquímica, Instituto de Química, Universidade de São Paulo, São Paulo 05508-900, Brazil;* orcid.org/0000-0002-2114-3815

Hernan Chaimovich − *Departamento de Bioquímica, Instituto de Química, Universidade de São Paulo, São Paulo 05508-900, Brazil;* orcid.org/0000-0001-9380-2157

Complete contact information is available at: https://pubs.acs.org/10.1021/acsanm.5c04519

Funding

The Article Processing Charge for the publication of this research was funded by the Coordenacao de Aperfeicoamento de Pessoal de Nivel Superior (CAPES), Brazil (ROR identifier: 00x0ma614).

Notes

The authors declare no competing financial interest.

■ ACKNOWLEDGMENTS

N.L.B.Z. Ph.D. thesis research is supported by the National Council for Scientific and Technological Development (CNPq project No 161545/2021-1). H.U. acknowledges funding for his work on tumor-targeting aptamers by the São Paulo Research

Foundation (FAPESP project No. 2023/17147-6). Y.Y.S.T. Ph.D. thesis research is supported by the National Council for Scientific and Technological Development (CNPq project No FUSP 3719). B.S.C. thanks FAPESP (2019/07634-1, 2023/01092-8, 2025/03447-3) and CNPq (141855/2019-3) for financial support. I.M.C. acknowledges CNPq, project No. 304155/2021-7; CNPq− 465259/2014-6; the Coordination for the Improvement of Higher Education Personnel (CAPES); the National Institute of Science and Technology Complex Fluids (INCT-FCx); and the São Paulo Research Foundation (FAPESP − 2014/50983-3). K.A. acknowledges the research funding by the National Council for Scientific and Technological Development (CNPq MAI/DAI No. 403663/2020-2) and PIPAE USP 2021.1.10424.1.9 for the project on hybrid nanomaterials for theranostics (nanoTera). F.C.M. acknowledges funding from FAPESP (2018/14898-2).

REFERENCES

(1) Bray, F.; Laversanne, M.; Sung, H.; Ferlay, J.; Siegel, R. L.; Soerjomataram, I.; Jemal, A. Global Cancer Statistics 2022: GLOBOCAN Estimates of Incidence and Mortality Worldwide for 36 Cancers in 185 Countries. *CA Cancer J. Clin* **2024**, *74* (3), 229−263.
(2) Zappa, C.; Mousa, S. A. Non-Small Cell Lung Cancer: Current Treatment and Future Advances. *Transl Lung Cancer Res.* **2016**, *5* (3), 288−300.
(3) American Cancer Society. *Treatment Choices for Non-Small Cell Lung Cancer, by Stage*; American Cancer Society 2017.
(4) Dasari, S.; Bernard Tchounwou, P. Cisplatin in Cancer Therapy: Molecular Mechanisms of Action. *Eur. J. Pharmacol.* **2014**, *740*, 364−378.
(5) Wang, D.; Lippard, S. J. Cellular Processing of Platinum Anticancer Drugs. *Nat. Rev. Drug Discov* **2005**, *4* (4), 307−320.
(6) Jeong, Y.-H.; Shin, H.-W.; Kwon, J.-Y.; Lee, S.-M. Cisplatin-Encapsulated Polymeric Nanoparticles with Molecular Geometry-Regulated Colloidal Properties and Controlled Drug Release. *ACS Appl. Mater. Interfaces* **2018**, *10* (28), 23617−23629.
(7) Moura, M. J.; Gil, M. H.; Figueiredo, M. M. Cisplatin Delivery Systems Based on Different Drug Encapsulation Techniques. *Eur. Polym. J.* **2019**, *113*, 357−364.
(8) Oliveira, M.; Leite, E.; Souza; Carvalho-Junior; Coelho; Lana, A.; Cassali. Encapsulation of Cisplatin in Long-Circulating and PH-Sensitive Liposomes Improves Its Antitumor Effect and Reduces Acute Toxicity. *Int. J. Nanomedicine* **2012**, 5259.
(9) Maeda, H.; Wu, J.; Sawa, T.; Matsumura, Y.; Hori, K. Tumor Vascular Permeability and the EPR Effect in Macromolecular Therapeutics: A Review. *J. Controlled Release* **2000**, *65* (1−2), 271−284.
(10) Ramachandran, S.; Quist, A. P.; Kumar, S.; Lal, R. Cisplatin Nanoliposomes for Cancer Therapy: AFM and Fluorescence Imaging of Cisplatin Encapsulation, Stability, Cellular Uptake, and Toxicity. *Langmuir* **2006**, *22* (19), 8156−8162.
(11) Boulikas, T. Clinical Overview on Lipoplatin ™: A Successful Liposomal Formulation of Cisplatin. *Expert Opin Investig Drugs* **2009**, *18* (8), 1197−1218.
(12) Yasemian, A. R.; Almasi Kashi, M.; Ramazani, A. Surfactant-Free Synthesis and Magnetic Hyperthermia Investigation of Iron Oxide (Fe3O4) Nanoparticles at Different Reaction Temperatures. *Mater. Chem. Phys.* **2019**, *230*, 9−16.
(13) Mahmoudi, M.; Sant, S.; Wang, B.; Laurent, S.; Sen, T. Superparamagnetic Iron Oxide Nanoparticles (SPIONs): Development, Surface Modification and Applications in Chemotherapy. *Adv. Drug Deliv Rev.* **2011**, *63* (1−2), 24−46.
(14) Bozzuto, G.; Molinari, A. Liposomes as Nanomedical Devices. *Int. J. Nanomedicine* **2015**, 975.
(15) Levy-Nissenbaum, E.; Radovic-Moreno, A. F.; Wang, A. Z.; Langer, R.; Farokhzad, O. C. Nanotechnology and Aptamers: Applications in Drug Delivery. *Trends Biotechnol* **2008**, *26* (8), 442−449.
(16) Sun, H.; Zu, Y. A Highlight of Recent Advances in Aptamer Technology and Its Application. *Molecules* **2015**, *20* (7), 11959−11980.
(17) Chehelgerdi, M.; Chehelgerdi, M.; Allela, O. Q. B.; Pecho, R. D. C.; Jayasankar, N.; Rao, D. P.; Thamaraikani, T.; Vasanthan, M.; Viktor, P.; Lakshmaiya, N.; Saadh, M. J.; Amajd, A.; Abo-Zaid, M. A.; Castillo-Acobo, R. Y.; Ismail, A. H.; Amin, A. H.; Akhavan-Sigari, R. Progressing Nanotechnology to Improve Targeted Cancer Treatment: Overcoming Hurdles in Its Clinical Implementation. *Mol. Cancer* **2023**, *22* (1), 169.
(18) Das, S.; Dey, S.; Patra, S.; Bera, A.; Ghosh, T.; Prasad, B.; Sayala, K. D.; Maji, K.; Bedi, A.; Debnath, S. *BODIPY-Based Molecules for Biomedical Applications. Biomolecules* **2023**, *13* (12), 1723.
(19) Kumar, P. P. P.; Saxena, S.; Joshi, R. BODIPY Dyes: A New Frontier in Cellular Imaging and Theragnostic Applications. *Colorants* **2025**, *4* (2), 13.
(20) Garcia-Osorio, D.; P. Nogueira, H.; Gonçalves, J. M.; Toma, S. H.; Garcia-Segura, S.; Araki, K. SPION-Decorated Organofunctionalized MCM48 Silica-Based Nanocomposites for Magnetic Solid-Phase Extraction. *Mater. Adv.* **2021**, *2* (3), 963−973.
(21) Toma, S. H.; Santos, J. J.; Araki, K.; Toma, H. E. Pushing the Surface-Enhanced Raman Scattering Analyses Sensitivity by Magnetic Concentration: A Simple Non Core−Shell Approach. *Anal. Chim. Acta* **2015**, *855*, 70−75.
(22) Toma, S. H.; Santos, J. J.; da Silva, D. G.; Huila, M. F. G.; Toma, H. E.; Araki, K. Improving Stability of Iron Oxide Nanofluids for Enhanced Oil Recovery: Exploiting Wettability Modifications in Carbonaceous Rocks. *J. Pet Sci. Eng.* **2022**, *212*, No. 110311.
(23) Peffi Ferreira, L. F.; Mazzi de Oliveira, T.; Toma, S. H.; Toyama, M. M.; Araki, K.; Avanzi, L. H. Superparamagnetic Iron Oxide Nanoparticles (SPIONs) Conjugated with Lipase *Candida Antarctica* A for Biodiesel Synthesis. *RSC Adv.* **2020**, *10* (63), 38490−38496.
(24) Sun, C.; Lee, J. S. H.; Zhang, M. Magnetic Nanoparticles in MR Imaging and Drug Delivery. *Adv. Drug Deliv Rev.* **2008**, *60* (11), 1252−1265.
(25) Cugnasca, B. S.; Wodtke, F.; Santos, A. A. D. Seleno-Functionalization of BODIPY Fluorophores Assisted by Oxidative Nucleophilic Hydrogen Substitution. *Curr. Chem. Biol.* **2021**, *15* (3), 215−221.
(26) Cugnasca, B. S.; Junior, T. C. T.; Penna, T. C.; Zuluaga, N. L. B.; Bustos, S. O.; Chammas, R.; Cuccovia, I. M.; Correra, T. C.; Dos Santos, A. A. Seleno-BODIPY as a Fluorescent Sensor for Differential and Highly Selective Detection of Cysteine and Glutathione for Bioimaging in HeLa Cells. *Dyes Pigm.* **2025**, *236*, No. 112658.
(27) Cugnasca, B. S.; Duarte, F.; Santos, H. M.; Capelo-Martínez, J. L.; Bértolo, E.; Dos Santos, A. A.; Lodeiro, C. Ammonia and Temperature Sensing Applications Using Fluorometric and Colorimetric Microparticles and Polymeric Films Doped with BODIPY-Emitters. *Microchimica Acta* **2024**, *191* (12), 746.
(28) Vidic, M.; Smuc, T.; Janez, N.; Blank, M.; Accetto, T.; Mavri, J.; Nascimento, I. C.; Nery, A. A.; Ulrich, H.; Lah, T. T. In Silico Selection Approach to Develop DNA Aptamers for a Stem-like Cell Subpopulation of Non-Small Lung Cancer Adenocarcinoma Cell Line A549. *Radiol Oncol* **2018**, *52* (2), 152−159.
(29) Rouser, G.; Fleischer, S.; Yamamoto, A. Two Dimensional Thin Layer Chromatographic Separation of Polar Lipids and Determination of Phospholipids by Phosphorus Analysis of Spots. *Lipids* **1970**, *5* (5), 494−496.
(30) Manzini, M. C.; Perez, K. R.; Riske, K. A.; Bozelli, J. C.; Santos, T. L.; da Silva, M. A.; Saraiva, G. K. V.; Politi, M. J.; Valente, A. P.; Almeida, F. C. L.; Chaimovich, H.; Rodrigues, M. A.; Bemquerer, M. P.; Schreier, S.; Cuccovia, I. M. Peptide:Lipid Ratio and Membrane Surface Charge Determine the Mechanism of Action of the Antimicrobial Peptide BP100. Conformational and Functional Studies. *Biochimica et Biophysica Acta (BBA) - Biomembranes* **2014**, *1838* (7), 1985−1999.
(31) Carvalho Júnior, A. D.; Vieira, F. P.; De Melo, V. J.; Lopes, M. T. P.; Silveira, J. N.; Ramaldes, G. A.; Garnier-Suillerot, A.; Pereira-Maia, E. C.; De Oliveira, M. C. Preparation and Cytotoxicity of Cisplatin-

https://doi.org/10.1021/acsanm.5c04519
ACS Appl. Nano Mater. 2026, 9, 2204−2217

Containing Liposomes. *Braz. J. Med. Biol. Res.* **2007**, *40* (8), 1149−1157.
(32) Basotra, M.; Singh, S. K.; Gulati, M. Development and Validation of a Simple and Sensitive Spectrometric Method for Estimation of Cisplatin Hydrochloride in Tablet Dosage Forms: Application to Dissolution Studies. *ISRN Analytical Chemistry* **2013**, *2013*, 1−8.
(33) Mosmann, T. Rapid Colorimetric Assay for Cellular Growth and Survival: Application to Proliferation and Cytotoxicity Assays. *J. Immunol Methods* **1983**, *65* (1−2), 55−63.
(34) MilliporeSigma. *MTT Cell Growth Assay Kit Protocol (Catal. No. CT02)*.https://www.merckmillipore.com/IL/en/product/mm/ct02.
(35) Mojsoska, B.; Zuckermann, R. N.; Jenssen, H. Structure-Activity Relationship Study of Novel Peptoids That Mimic the Structure of Antimicrobial Peptides. *Antimicrob. Agents Chemother.* **2015**, *59* (7), 4112−4120.
(36) Peffi Ferreira, L. F.; Mazzi de Oliveira, T.; Toma, S. H.; Toyama, M. M.; Araki, K.; Avanzi, L. H. Superparamagnetic Iron Oxide Nanoparticles (SPIONs) Conjugated with Lipase Candida Antarctica A for Biodiesel Synthesis. *RSC Adv.* **2020**, *10* (63), 38490−38496.
(37) Honary, S.; Zahir, F. Effect of Zeta Potential on the Properties of Nano-Drug Delivery Systems - A Review (Part 1). *Trop. J. Pharm. Res.* **2013**, *12* (2), 255.
(38) Barbasz, A. M.; Dyba, B. Direct Interaction of Zirconia Nanoparticles with Human Immune Cells. *Biophysica* **2024**, *4* (1), 83−91.
(39) Mura, S.; Nicolas, J.; Couvreur, P. Stimuli-Responsive Nanocarriers for Drug Delivery. *Nat. Mater.* **2013**, *12* (11), 991−1003.
(40) Shi, J.; Kantoff, P. W.; Wooster, R.; Farokhzad, O. C. Cancer Nanomedicine: Progress, Challenges and Opportunities. *Nat. Rev. Cancer* **2017**, *17* (1), 20−37.
(41) Wang, J.-P.; Huang, Z.-R.; Zhang, C.; Ni, Y.-R.; Li, B.-T.; Wang, Y.; Wu, J.-F. Methodological Advances in Liposomal Encapsulation Efficiency Determination: Systematic Review and Analysis. *J. Drug Target* **2025**, 1−10.
(42) Plourde, K.; Derbali, R. M.; Desrosiers, A.; Dubath, C.; Vallée-Bélisle, A.; Leblond, J. Aptamer-Based Liposomes Improve Specific Drug Loading and Release. *J. Controlled Release* **2017**, *251*, 82−91.
(43) Yu, S.; Zhang, H.; Zhang, S.; Zhong, M.; Fan, H. Ferrite Nanoparticles-Based Reactive Oxygen Species-Mediated Cancer Therapy. *Front. Chem.* **2021**, *9*, No. 651053.
(44) Elmorsy, E. A.; Saber, S.; Hamad, R. S.; Abdel-Reheim, M. A.; Elkott, A. F.; AlShehri, M. A.; Morsy, K.; Salama, S. A.; Youssef, M. E. Advances in Understanding Cisplatin-Induced Toxicity: Molecular Mechanisms and Protective Strategies. *European Journal of Pharmaceutical Sciences* **2024**, *203*, No. 106939.
(45) Oh, G. S.; Kim, H. J.; Shen, A.; Lee, S. B.; Khadka, D.; Pandit, A.; So, H. S. Cisplatin-Induced Kidney Dysfunction and Perspectives on Improving Treatment Strategies. *Electrolyte Blood Press* **2014**, *12* (2), 55−65.
(46) Mody, M. D.; Gill, H. S.; Higgins, K. A.; Saba, N. F.; Kota, V. K. Complete Remission of Acute Myeloid Leukemia Following Cisplatin Based Concurrent Therapy with Radiation for Squamous Cell Laryngeal Cancer. *Case Rep. Hematol.* **2016**, *2016*, 1.
(47) Geoghegan, F.; Buckland, R. J.; Rogers, E. T.; Khalifa, K.; O'Connor, E. B.; Rooney, M. F.; Behnam-Motlagh, P.; Nilsson, T. K.; Grankvist, K.; Porter, R. K. Bioenergetics of Acquired Cisplatin Resistant H1299 Non-Small Cell Lung Cancer and P31 Mesothelioma Cells. *Oncotarget* **2017**, *8* (55), 94711−94725.
(48) Stoltenburg, R.; Reinemann, C.; Strehlitz, B. SELEX—A (r)Evolutionary Method to Generate High-Affinity Nucleic Acid Ligands. *Biomol Eng.* **2007**, *24* (4), 381−403.
(49) Kaur, H.; Yung, L.-Y. L. Probing High Affinity Sequences of DNA Aptamer against VEGF165. *PLoS One* **2012**, *7* (2), No. e31196.
(50) Torchilin, V. P. Multifunctional, Stimuli-Sensitive Nanoparticulate Systems for Drug Delivery. *Nat. Rev. Drug Discov* **2014**, *13* (11), 813−827.
(51) Fan, Z.; Fu, P. P.; Yu, H.; Ray, P. C. Theranostic Nanomedicine for Cancer Detection and Treatment. *J. Food Drug Anal* **2014**, *22* (1), 3−17.

https://doi.org/10.1021/acsanm.5c04519
ACS Appl. Nano Mater. 2026, 9, 2204−2217